RSC Advances

PAPER

View Article Online
View Journal | View Issue

Check for updates

Cite this: *RSC Adv.*, 2026, **16**, 723

Small buds to blooming flowers: organic–inorganic hybrid nanoflowers as immobilization platform and robust system for bio-catalytic production of D-allose

Sweety Sharma,[ab] Shantanu B. Sathaye,[ac] Yeddula Nikhileshwar Reddy,[a] Jayeeta Bhaumik[a] and Sudhir Pratap Singh*[ac]

Received 19th August 2025
Accepted 16th December 2025

DOI: 10.1039/d5ra06127j

rsc.li/rsc-advances

D-Allose is a rare monosaccharide and a low-calorie sweetener found in tiny amounts in nature with potential health benefits. Its scarcity in nature and high production cost pose a challenge to industry. The enzymatic route for D-allose production using L-rhamnose isomerase (L-RI$_M$) is a promising and sustainable approach. The sensitivity of the enzyme to pH and temperature limits its application. In this study, we have developed manganese-based hybrid micro-structures (L-RI$_{Mn}$NFs) that offer robustness and recyclability to the enzymatic process of D-allose biosynthesis. The hybrid of organic and inorganic microstructure attains flower-like morphology, with each petal in the nanometer dimensions as visualized under electron microscopy. Molecular dynamics (MD) simulations were performed to understand the formation of these flower-like structures. These nanoflowers (NFs) exhibited better kinetic properties and reusability, retaining almost >60% activity even after the 6th cycle of reaction. So far, this study is the first attempt to immobilize L-rhamnose isomerase enzyme onto hybrid nanoflowers (hNFs) and to conduct simulation studies thereof. It provides insights into the improved robustness and durability of L-RI$_M$ after immobilization with a turnover number of 679.9 s^{-1}. These NFs can be developed into biocatalytic platforms for the production of rare sugars.

1. Introduction

D-Allose is a rare monosaccharide and an epimer of D-glucose, differing only at C3 position of D-glucose. Though it is a naturally occurring sugar, it exists in minimal quantities in nature. Like many other rare sugars, this monosaccharide is a potential candidate for a low-calorie sweetener and a functional ingredient in therapeutic interventions. Various studies have endorsed the prospective uses of D-allose as a cryo-protectant,[1] anti-oxidant,[2] anti-microbial,[3] anti-inflammatory,[4] tumor suppressive,[5] and immuno-suppressive[6,7] agent. In view of wide applications of D-allose, it is desirable to develop processes for the continuous production of this biomolecule. D-Allulose is another important rare sugar used as substrate for D-allose production. Global D-allulose production ranges approximately 283.4 million dollars with CAGR of 8.6%. However, D-allose production at industrial level is still in infancy due to its limited production.[8] The biological or enzymatic route of production is preferable over chemical synthesis of the molecule, as the former offers high specificity and better yield without the use of corrosive agents, making the process environment-friendly.[9]

L-Rhamnose isomerase is a potential enzyme for D-allose production.[10] It is a multi-substrate enzyme with the highest specificity for L-rhamnose. Though this enzyme is capable of catalyzing the isomerization of many other monosaccharides like D-glucose, L-glucose, D-galactose, D-mannose, it has been well characterized for D-allose production.[11] Generally, biocatalysts offer high specificity, low toxicity, high activity and high product yield under mild conditions. However, many enzymatic processes face the disadvantages associated with reusability and the functionality of the biocatalyst under harsh industrial conditions. Immobilization of enzyme molecules to a suitable matrix makes the bio-catalytic process robust and economical, conferring elevated stability and multiple catalytic cycles.[12,13] Many reports have documented that immobilization leads to a better kinetics of the enzyme.[14,15] Immobilization of L-rhamnose isomerase has been demonstrated on Chitopearl beads,[16] anion exchange resins,[17] Duolite beads,[18] and as cross-linked clusters.[19] In the aforementioned studies, enzyme immobilization has been devised on organic, inorganic, and mixed matrices, following the approaches of adsorption, entrapment or encapsulation and covalent modification.[15,20]

---

[a] Center of Innovative and Applied Bioprocessing (BRIC-NABI), Sector 81, SAS Nagar, Mohali, India

[b] Indian Institute of Science Education and Research, Mohali, India

[c] Department of Industrial Biotechnology, Gujarat Biotechnology University, GIFT City, Gandhinagar, Gujarat 382355, India. E-mail: sudhir.singh@gbu.edu.in

Immobilization events may alter the active site of the enzyme, leading to decrease in activity and increased mass transfer.[21] The beads or resin carriers as immobilization platform are formed by conventional method *i.e.*, adsorption, physical entrapment or covalent binding for the enzyme immobilization. The conventional immobilization suffers with enzyme leaching and/or diminished activity of the enzyme, in turn decreasing the loading capacity and catalytic efficiency. Further, covalent immobilization may alter the active site and often catalytic performance of the enzyme is compromised.[22] Therefore, there is a need to follow alternative immobilization approaches for the improvement in bio-catalytic process without compromising the activity.[23] To tackle this issue, preparation of self-assembling protein structures are being explored. The bottom-up approach to form ordered nano- or micro-scale structures improves enzyme activity by providing reduced mass transfer resistance and diffusional constraints. These assemblies provide accessible microenvironments while preserving the native conformational state of the protein as compared to conventional immobilization methods.[12]

Nano-flowers are formed by self-assembly of protein molecules in the presence of metal and phosphate ions, preserving the native state of enzyme, reducing the usage of expensive conjugating agents, and in these structural conjugates leaching of enzymes is largely avoided. Interestingly, nanostructure allow a greater exposure to the enzymatic active site for proper channelling and increased accessibility of the substrate.[24,25]

Different 3D architectures for enzyme immobilization have innumerable applications due to additional benefits of decreased size, increased surface area and multiple interfaces. The structures formed by self-assembly have drawn attention of researchers in recent years due to multitude of advantages, such as easier method of preparation, enhanced selectivity, activity and stability of the enzymes.[12,26–29] The hybrid organic–inorganic flower-like structures, known as nanoflowers (NFs), are quite popular these days in the enzyme immobilization world.[30] These structures were first reported by Ge *et al.* 2012, where they synthesized different kinds of NFs by using copper phosphate ($Cu_3(PO_4)_2$) and a variety of proteins.[31] These structures were formed by self-assembly between the amine/carboxyl group of protein (organic component) and metal phosphates (inorganic component).[32] The synthesis takes place mainly in three steps: (1) nucleation: formation of primary crystals of metal and phosphate ions, (2) anisotropic growth: formation of coordination bonds between primary crystals and amino/carboxyl groups of side chains of amino acids of the enzyme, and (3) flower-like morphology: aggregation of petal-like nano-structures to form complete flower, where protein component acts as "adhesive" for sustaining such morphology. For metal dependent enzymes, it is an advantage to use inorganic component containing the desirable metal that acts as cofactor, enhancing the catalytic activity and structural integrity of the enzyme.

In the present investigation, we have immobilized L-rhamnose isomerase enzyme as an organic component into self-assembled flower-like structures, using manganese as inorganic component, to form a hybrid system. Different characterisation studies were performed to elucidate the structural and physical aspects of these structures. A simulation-based approach was used to get insights into possible mechanism involved in formation of these structures. Biochemical characterization of the NF structures was conducted to study catalytic efficiency, specificity and reusability of enzyme. This combinatorial platform is presumably a smart solution for the industrial production of rare sugars of high-value, such as D-allose.

2. Experimental section

2.1. Materials

Yeast extract, kanamycin sulphate, tris-base, bromophenol blue, Coomassie brilliant blue R250, sodium dodecyl sulphate, isopropyl β-D-thiogalactoside, (IPTG), and fluorescein isothiocynate (FITC) were purchased from Merck/Sigma-Aldrich (Darmstadt, Germany). Manganese sulphate, sodium chloride, potassium chloride, potassium phosphate monobasic and sodium phosphate dibasic were procured from Himedia (Maharashtra, India) and Sigma-Aldrich (Darmstadt, Germany). D-Allulose was purchased from Splenda, USA. Premixed dual color protein ladder was purchased from Bio-Rad (California, USA). The enzyme Q5 DNA polymerase was obtained from Thermo Fisher Scientific (MA, USA) and the restriction enzymes were purchased from NEB. The pET28a (+) shuttle vector was procured from Novagen (Darmstadt, Germany). *Escherichia coli* Top 10 and *E. coli* BL21 (DE3) strains were purchased from Invitrogen (Waltham, MA, USA).

2.2. Methods and instruments

The complete structural characterization of the hNFs was carried out. The morphological details of L-rhamnose isomerase manganese-nanoflowers (L-RI_{Mn}NFs) were visualized by scanning electron microscopy (SEM), the size distribution of NFs was determined by dynamic light scattering (DLS). The functional groups were studied by Fourier Transform Infrared (FTIR) spectroscopy. Crystallinity was analysed by Powder X-ray Diffraction (PXRD) while pore size distribution was done using Brunauer–Emmett–Teller (BET) analysis. Differential Scanning Calorimetry/Thermogravimetric Analysis (DSC/TGA) was performed to get the thermal insights of the prepared structures. Further validation of successful hybrid formation was done using Confocal Laser Scanning Microscopy (CLSM), and UV-Visible spectrophotometric analysis. Transmission electron microscopy was performed to get fine structural details, and the elemental distribution was analysed by field emission-SEM (FE-SEM) equipped with energy dispersive X-ray (EDX).

The qualitative and quantitative analysis of loaded protein was performed by recording spectrophotometric absorbance and Bradford assay (Sigma-Aldrich, St. Louis, Missouri) by using bovine serum albumin (BSA) as a standard. Detailed method is provided in SI Section 2.2 and Fig. S2.

For functional group analyses, L-RI_{Mn}NFs samples were dried using lyophilyzer for 24 h. Then, each sample was applied onto the surface provided for sample analysis. The structural details were determined by Fourier transform infrared spectrophotometry (FT-IR) in the spectral range of 4000 to 400 cm^{-1} [attenuated total reflection (ATR) mode].

The crystallinity of the lyophilized hNFs along with other controls was determined by powder X-ray diffraction crystallography (XRD). The Cu Kα radiations (λ = 1.540593) were recorded at 40 kV voltage of diffractometer and in a scan range of 5–80 θ with a scan speed of 5° min^{-1}. To validate the thermal stability of NFs, differential scanning calorimetry (DSC)/thermal gravimetric analysis (TGA) was done using ~7 mg of freeze-dried sample. The analysis was carried out in the range of 30 °C to 600 °C, with a consistent heating rate of 15 °C min^{-1}.

The Brunauer–Emmett–Teller (BET) analysis was carried out to measure the specific surface area (BET-SSA) and porosity of the synthesised nanocomposites. The synthesised NFs were degassed at 100 °C for around 2 h prior to analysis.

The size distribution of NFs was determined by DLS. The surface charge distribution of protein–metal complex was determined by measuring zeta potential of the NFs. The association of protein component with metal phosphates in the NFs and the uniformity of distribution were determined by fluorescent dye (FITC) tagging. For this, 50 µl of FITC (1 mg ml^{-1} in DMSO) was added to the enzyme followed by incubation at 4 °C with slow shaking for 8–12 hours. The tagged protein was then used for the NF synthesis and later monitored by confocal laser scanning microscopy (CLSM).

2.3. Cloning, expression and purification of recombinant enzyme

The heterologous expression of the recombinant metagenomic L-rhamnose isomerase (L-RI_M) was performed as described in our previous report.[33] Briefly, the gene was cloned in the expression vector, pET28a, with his-tag at C-terminus, and transferred to the expression host *E. coli* BL21 (DE3) for protein production. The detailed information about gene cloning, transformation, expression and purification of recombinant protein is provided in SI (Section S2.1).

2.4. Preparation of L-rhamnose isomerase manganese-nanoflowers (L-RI_MnNFs)

The hNFs were prepared by using organic, *i.e.*, protein (L-RI_M), and inorganic, *i.e.* metal ions (manganese sulphate and phosphate), components. The enzyme concentrations, incubation period, *etc.*, were optimized for obtaining stable structure and desirable enzyme activity. The growth of nano-assemblies was observed at different incubation times (0, 12, 24, 48, 72, and 86 h). In the early stages, tiny metal and phosphate crystals started forming. With time, the nanopetals expanded sideways, reaching a certain length. After around 48 h, these petals aligned in a uniform way, achieving a flower-like shape. Detailed description is provided in SI (Section S2.2). About 0.2 mg ml^{-1} of purified L-RI_M protein was added to 10 ml phosphate buffered saline (PBS) (1×, pH 7.4) and mixed thoroughly. Then, 1 mM manganese sulphate was added and gently mixed. The mixture was incubated at 4 °C, and left undisturbed for about 48 h. The white precipitate of NFs preparation was washed with PBS 2–3 times to remove excess of enzyme and metal salt, and then, recollected by centrifugation at 12 000 RPM for 20 min, followed by re-suspension in 50 mM HEPES buffer. The prepared NFs were stored at 4 °C till further use.

2.5. Molecular dynamics (MD) simulation studies of L-RI_MnNFs

The influence of metal ions on the self-assembly of L-RI_M into a NF structure was examined through molecular dynamics (MD) simulations, designed to mimic the NF formation process. To design the simulation systems, the predicted three-dimensional structure of L-RI_M, Mn^{2+} and PO_4^{2-} ions were used in the ratio of 1 : 50 : 50, respectively. The monomeric protein structure of L-RI_M was obtained from the AlphaFold2 structure prediction tool. The simulation was performed using the tool, GROMACS 2020.1.[34] The simulations used the CHARMM36[35] force field. A dodecahedron-shaped simulation box was created with a 1 nm periodic boundary condition and filled with water molecules as the solvent. The total charge on the system was neutralized using Na^+ or Cl^- ions. The energy of the system was minimized using the steepest descent minimization algorithm.[36] The systems were equilibrated under *NVT* (constant number of particles, volume, and temperature) for 2000 ps, followed by *NPT* (constant number of particles, pressure, and temperature). After the completion of both equilibration steps, MD run was performed for 100 ns. The LINCS algorithm was used for the covalent bond constraints. The electrostatic interactions were treated with the Particle Mesh Ewald (PME) method.[37,38] The designed systems were simulated at two different temperature points, 4 °C and 25 °C, to evaluate the effect of temperature on the self-assembly of metal–protein structure. A protein simulation system, without any addition of the metal ion, was used as a control system (Table S1).

Each trajectory after the completion of MD run was analyzed using the Gromacs utilities. The root mean square deviation (RMSD), solvent-accessible surface area (SASA), and radius of gyration (R_g) was computed by using 'gmx rms,' 'gmx sasa,' and 'gmx gyrate' Gromacs utilities, respectively.[39,40] The XMgrace tool was used to prepare the graphs.[41]

2.6. Activity assays

The enzyme assays were conducted in 20 mM HEPES buffer (pH 7.0), taking 10 mM D-allulose treated with 0.1 mg ml^{-1} L-RI_MnNFs for 10 min. Any additional metal co-factor was not used in the enzymatic reactions. After completion of the assay, the reaction mix was incubated on ice for 1 min, followed by centrifugation at 12 000 RPM/25 °C for 20 min to separate the NFs and stop the reaction. The separated supernatant was further boiled at 100 °C for 5 min to assure complete denaturation of the leached enzyme, if any. The mixture was further centrifuged and filtered through 0.2 µm filter. The filtered samples were diluted in 50% acetonitrile: water followed by analysis in HPLC (Agilent technologies) equipped with Zorbax-NH2 column and refractive index detector (RID). The column and the detector temperature were 40 °C and 45 °C, respectively. The mobile phase was acetonitrile and MilliQ water (mixed at 65 : 35 ratio), with a flow rate of 1 ml min^{-1}.

2.7. Biochemical characterization of L-RI_MnNFs

For determining the effect of different temperatures on activity of immobilized L-RI_M, enzyme assays were performed at temperatures ranging from 50 to 100 °C, and pH 7.0. For determining the pH optima, enzyme assays were carried out in the pH range of 5.0 to 10.0 by using different buffers (20 mM), *e.g.*, sodium acetate (pH 4.0 to 5.5), sodium phosphate (pH 6.0 to 6.5), HEPES (pH 7.0 to 8.5), and glycine-NaOH (pH 9.0 to 10.0). The pH stability was assessed by incubating the freshly prepared NFs at pH 6.0 to 9.0 (using the aforementioned buffers) for 2 h at room temperature, followed by enzyme activity assay.

2.8. Kinetic properties of L-RI$_{\mathrm{Mn}}$NFs

Enzyme kinetics studies of immobilized L-RI$_{\mathrm{M}}$ were performed by conducting enzyme activity assays, taking different concentrations (10 mM to 400 mM) of D-allulose. The Michaelis–Menten constant (K_{m}) and V_{max} values were calculated using the Lineweaver–Burk plot.

2.9. Reusability of prepared L-RI$_{\mathrm{Mn}}$NFs

For determining the strength of the self-assembled structures, reusability test of the NFs was accomplished by performing multiple duty cycles of reaction. The L-RI$_{\mathrm{Mn}}$NFs were recovered by centrifugation after completion of the reaction. The protein leached into supernatant after each cycle was quantified by Bradford assay.

2.10. Time point conversion

D-Allose production was determined at different time points by incubating the reaction mixture for 120 min, with periodic procurement and quantification of the reaction product after every 10 min.

3. Result and discussion

3.1. Cloning, expression and purification of enzyme

The gene for L-rhamnose isomerase (L-RI$_{\mathrm{M}}$) was heterologously expressed in *E. coli* BL21 (DE3), and the protein was purified *via* affinity chromatography.[33] The visualization of protein on SDS-PAGE depicted more than 95% purity (Fig. S1).

3.2. Synthesis of L-RI$_{\mathrm{Mn}}$NFs

The complexion of phosphate buffered saline and the protein (L-RI$_{\mathrm{M}}$) with manganese sulphate resulted into synthesis of hybrid NFs (Fig. 1). The size and morphology of these structures depend on various factors like enzyme concentration, incubation time, *etc.*[31] (Fig. S3 and S4).

SEM images of different stages of NF synthesis, and the effect of trypsin, EDTA, different enzyme concentrations, temperature and incubation period on NF's formation have been elaborated in SI Section 2.3. The optimization of NF synthesis was done by using different enzyme and/or metal salt concentrations and incubated for different time periods (Section S2.2, Fig. S3 and S4). The NF of desirable morphology and activity could be obtained by using 0.2 mg ml^{-1} enzyme, pH 7.4, and incubation at 4 °C for 48 h. The SEM and TEM analysis depicted the flower-like morphology of the nano-clusters (Fig. 2A–D).

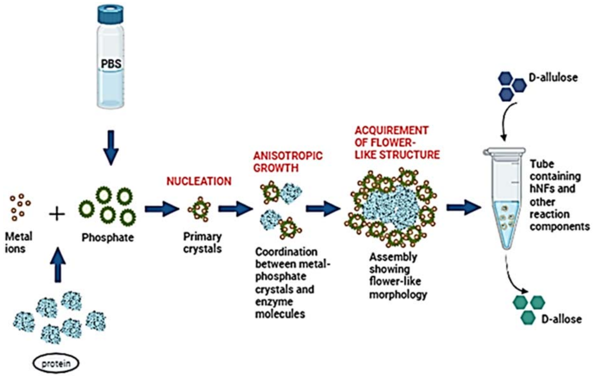

Fig. 1 Stepwise synthesis of self-assembled NFs.

3.3. MD simulation of L-RI$_{\mathrm{Mn}}$NFs assembly

To understand the process of the self-assembling of NFs and to clarify the role of ions facilitating the NFs' synthesis, molecular dynamic simulation studies were performed. The RMSD analysis of the simulation trajectory suggests conformational changes as well as structural stability of the protein.[37] All the simulation trajectories exhibited stabilization with time, suggesting that each system has achieved structural equilibrium (Fig. S5A and B). This also indicated reliability of the simulation process. The average RMSD values of simulation systems, 'Test_4' (simulation of L-RI$_{\mathrm{M}}$ with Mn^{2+} and $\mathrm{PO_4}^{2-}$ ions performed at 4 °C) and 'Test_25' (simulation of L-RI$_{\mathrm{M}}$ with Mn^{2+} and $\mathrm{PO_4}^{2-}$ ions performed at 25 °C) were computed to be 0.23 ± 0.03 nm and 0.41 ± 0.13 nm, respectively (Fig. S5B).

The average RMSD value of the 'Test_4' system was found lower as compared to that of 'Test_25', signifying higher conformational stability of protein at 4 °C. The results are in agreement with the experimental data (Fig. S3 and S4) for the synthesis of the NFs.

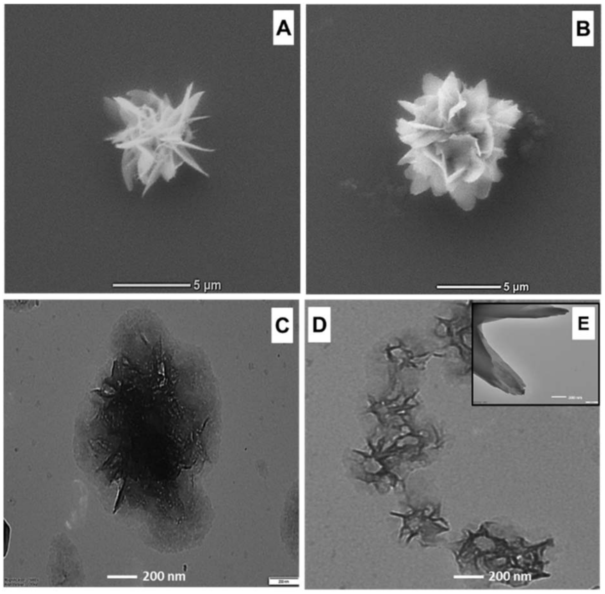

Fig. 2 (A) SEM image after incubation at 25 °C (RT), (B) SEM image after incubation at 4 °C, (C) TEM image of a single NF, (D) TEM image of the cluster of NFs, and (E) TEM image of magnified petals in the inset.

The simulation systems, 'Test_4' and 'Control_4' (simulation of L-RI$_{\mathrm{M}}$ only at 4 °C), were compared to investigate the possible impact of Mn^{2+} and PO$_4^{2-}$ ions on the synthesis of NFs at 4 °C. The RMSD trajectory analysis of 'Test_4' system was observed to attain a plateau at around 30 ns onwards, with minor fluctuations. This indicates that the protein complex system has achieved equilibrium for the synthesis of the hybrid nanoflowers. The snapshots at different time intervals (*i.e.*, 0 ns, 30 ns, and 100 ns) displayed the clustering of Mn^{2+} and PO$_4^{2-}$ ions around the protein surface with time (Fig. 3A), which could be critical in the formation of self-assembled NF structures. This observation motivated us to explore the surface composition of the protein surface with respect to the solvent accessibility. The computed average SASA value for 'Control_4' is 233.07 ± 1.823 nm^2, while for the 'Test_4' system, it was 230.84 ± 1.83 nm^2, indicating relatively reduced solvent accessibility.[42] Though there was a minute difference in the average SASA values, 'Test_4' system showed a pattern different from that of 'Control_4' in the simulation trajectory. 'Test_4' system showed a gradual decrease in the accessible area marking from 30 000 ps (*i.e.*, 30 ns) onwards, in contrast to 'Control_4' system (Fig. 3B). This implies the gradual reduction of protein backbone accessibility to the solvent molecules in the case of 'Test_4' system. This is possibly due to the formation of cluster of ions surrounding the protein surface. The self-assembling of metal ions and protein leads to increase the compactness of the structure.[43] The average radius of the gyration (R_g) of the 'Control_4' and 'Test_4' was noted to be 2.26 ± 0.01 nm and 2.24 ± 0.01 nm, respectively (Fig. 3C). The lower R_g in 'Test_4' system indicates increments in the compactness of the protein structure with time. Interestingly, protein-ion complexes showed a common pattern of surface metal ion clusters that can be visualized into 3 regions highlighted in Fig. 3D. In cluster I, the residues involved in binding with the phosphate and manganese ions were identified as GLU 20, ARG 21, GLU 386, LEU 383, ARG 367, ASP28, and ALA 24. Cluster II showed the metal binding residues as ARG 300 and ARG 297, while HIS 259, ASP 216, and GLU 213 were metal associated residues of cluster III. Besides these clustered residues, 4 residues were noticed to have metal interaction *viz.*, ARG 95, ASP 279, ASP 290, and ARG 76 (Fig. 3D). The results endorsed the essentiality of Mn^{2+} and PO$_4^{3-}$ ions in stabilizing the protein structure and facilitating self-assembly.

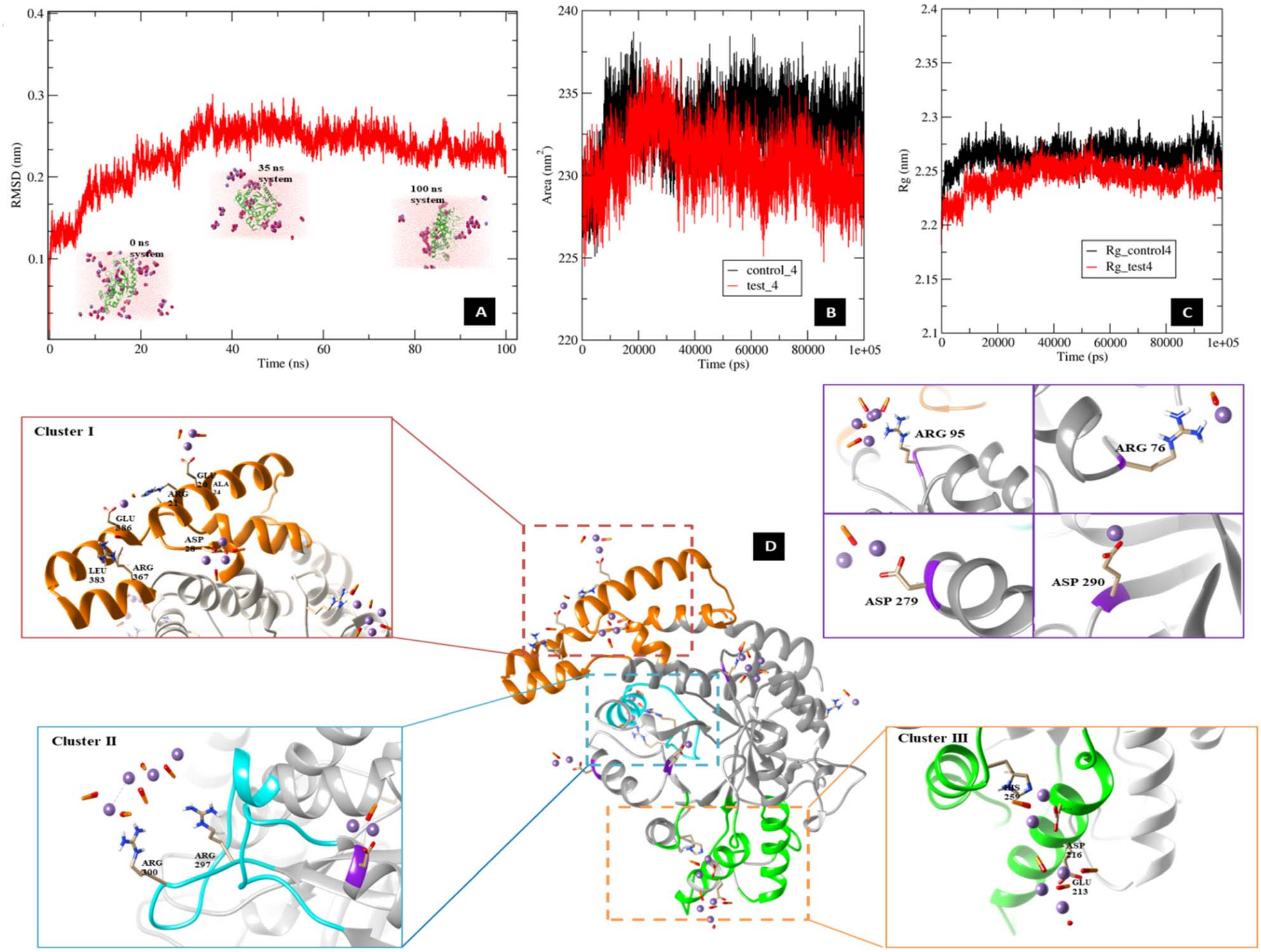

Fig. 3 Analysis for preparation of self-assembled L-RI$_{\mathrm{Mn}}$NFs synthesis using MD simulation trajectories. (A) RMSD values (nm) and the snapshots of the MD simulation for L-RI$_{\mathrm{Mn}}$NFs preparation at 4 °C, (B) solvent accessible surface area (SASA; nm^2) values for the control and the test systems at 4 °C of MD simulation, (C) values of the radius of gyration (R_g; nm) for the control and the test systems at 4 °C of MD simulation for the synthesis of the L-RI$_{\mathrm{Mn}}$NFs, (D) protein surface-metal ion clusters I, II and III, and other metal interacting residues (ARG 95, ASP 279, ASP 290, and ARG 76).

As immobilization of enzyme can induce changes in the conformation of a protein,[44] it is advisable to assess the possible changes in the protein sites critical for substrate binding and catalysis in nanoflower particles. The amino acid residues crucial for substrate binding (Glu233, Asp334, Asp267, and His294) in the protein-ion complex system (Fig. S5C) were found same as identified for the free form of the protein, L-RI$_M$.[33] In L-rhamnose isomerases, the evolutionarily conserved α1–β1 loop plays an important role in executing catalytic activity.[45] The superimposition of α1–β1 loop in simulated L-RI$_{Mn}$NFs and L-RI$_M$ in its free form displayed the RMSD value of 0.8 nm. The results infer that the simulated L-RI$_{Mn}$NFs did not exhibit any significant change in the conformation of evolutionarily conserved α1–β1 loop (Fig. S5D). This signifies that the process involved in the synthesis of NFs should not exert any undesirable impact on the catalytic activity of L-RI$_M$ (Table S1 and Fig. S5B).

3.4. Physical characterization of prepared L-RI$_{Mn}$NFs

The structural characterization of the hybrid nanoflowers (L-RI$_{Mn}$NFs) was done using SEM, FE-SEM, EDX, TEM, FTIR, XRD, DSC/TGA, DLS, CLSM, CD, and spectrophotometry. SEM analysis depicted flower-like surface morphology of the nanoflower particles of uniform size. The FE-SEM images measured the size of NFs in the range of 7–9 µm, with a few hundred nanometer-sized petals arranged in flower-like structure (Fig. 4A). The size range of NFs in this study is in line with the previous reports on transaminase NFs and trypsin NFs.[46,47] The EDX analysis revealed that NFs are majorly comprised of carbon (C), nitrogen (N), oxygen (O), sulphur (S) and manganese (Mn), with traces of phosphorus (P) (Fig. S6 and 4B, C).[48,49]

The presence of Mn and other elements indicated the prominent incorporation of protein component into NFs. The transmission electron microscopic (TEM) analysis presented the contrasting image of the petals, and the grooves formed by their assembly affirming the porosity of the structure (Fig. 2C and D). This gives the reason for high surface to volume ratio of these structures. TEM also confirmed the size range of 7–9 µm of NFs, while the petals were 400–500 nm in length. Similar images were reported by Rai *et al.* and Huang *et al.*[50,51]

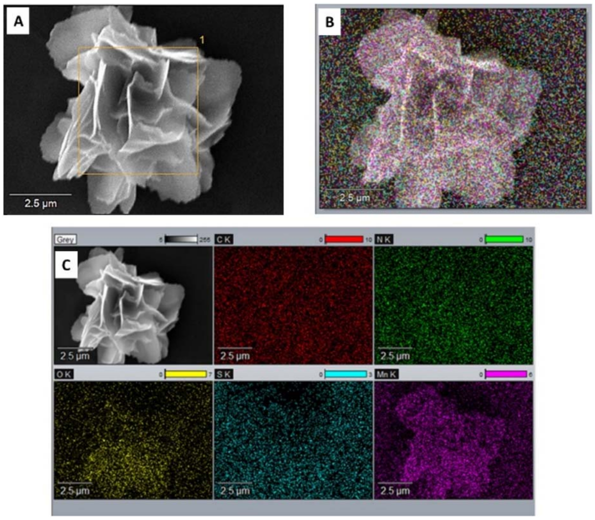

Fig. 4 (A and B) Scanning Electron Microscope (SEM) image of an individual NF (scale 2.5 µm), (B and C) Energy Dispersive X-ray (EDX) analysis determining the elemental distribution in an individual NF.

For gaining the structural details of immobilized L-RI$_M$ and chemical composition of NFs, FTIR in ATR mode was performed in wavelength range of 4000 to 400 cm^{-1}. The enzyme's FTIR spectra exhibited prominent absorption bands near 3267 cm^{-1}, attributed to O–H and N–H stretching vibrations, and characteristic of hydroxyl and amine groups in protein. This band, albeit with reduced intensity, can be noted in the enzyme nanoflower, suggesting the presence and attachment of the enzyme in the nanoflower. The prominent peak between 1600 and 1700 cm^{-1} corresponds to the amide I band (primarily C═O stretching), while a peak around 1540 cm^{-1} is indicative of the amide II band (mainly N–H bending and C–N stretching).[52] Furthermore, a distinct C–N (1250 cm^{-1}) stretching vibration, characteristic of protein or enzyme amide linkages, was importantly observed in the pure enzyme spectrum. This band appeared with reduced intensity in both the bare nanoflowers and the enzyme-nanoflower composite, indicating successful enzyme immobilization on the Mn nanoflower surface through weak covalent or electrostatic interactions. A small band nearly at 1633 cm^{-1} indicates bending vibration of O–H groups in the adsorbed water molecules. The presence of these amide bands in the conjugated sample confirms that the enzyme retains its structural features upon conjugation, indicating minimal denaturation. A broad peak observed between 500 and 650 cm^{-1} corresponds to the Mn–O stretching vibrations, confirming the presence of manganese oxide in the nanoflower structure. Moreover, Mn nanoflowers exhibit eminent peaks around ∼1070 cm^{-1} and ∼950–900 cm^{-1} due to P–O asymmetric stretching (PO_4^{3-}) and metal oxygen phosphate (Mn–O–P) vibrations. Additionally, the fingerprint region (500–1500 cm^{-1}), which contains complex and characteristic vibrational modes, shows several retained features in the conjugated sample. This further supports that the enzyme maintains its structural integrity and potentially remains functionally active when immobilized on the nanoflower surface.

The absorption bands at 1152 cm^{-1} corresponds to stretching vibration of P═O bond, 1049 cm^{-1} to asymmetrical stretching of P–O bond, 989 cm^{-1} to stretching vibration of P–O bond, 624 cm^{-1} to bending vibration of P–O bond and 553 cm^{-1} to in-plane bending vibration of phosphate ion, indicating the presence of phosphate groups.[53] Also, there was no significant peak shift in NF's spectra as compared to free enzyme control (Fig. 5A), indicating the self-assembled nature of synthesized nanostructures, possibly formed by coordination bond rather than covalent bonds.[54]

The crystallinity of the nanoflowers was analyzed by powder X-ray diffraction (PXRD). The relative peaks obtained in XRD of NFs showed similar pattern of peaks (Fig. 5B), as previously reported for $Mn_3(PO_4)_2 \cdot 3H_2O$ in the Inorganic Crystal Structure Database (ICSD) (JCPDS no. 00-003-0426). Since proteins are amorphous, the additional peaks could be attributed to the presence of phosphate along with manganese crystals.[45,49,51,55]

The absorption and desorption studies were carried out by using the Brunauer–Emmett–Teller (BET) analysis for specific surface area (SSA) and pore size determination.[46,56] Fig. S7A shows the N_2 adsorption/desorption isotherm of enzyme-

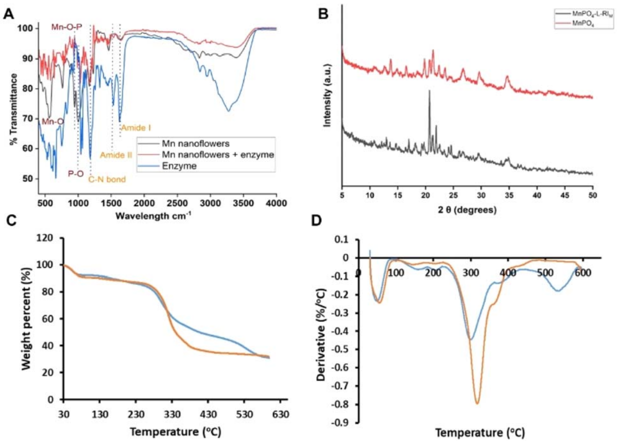

Fig. 5 Physical characterization of L-RIMnNFs. (A) FTIR analysis (B) XRD analysis, (C and D) TGA and DTG graphs (blue line: metal phosphate control; orange line: L-RI$_{Mn}$NFs.).

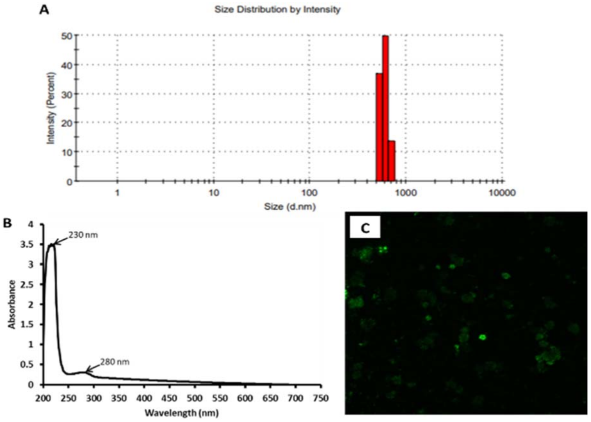

Fig. 6 Physical characterization of L-RI$_{Mn}$NFs. (A) DLS, (B) UV-vis spectrophotometry, and (C) CLSM activity assay and product analysis of L-RIMn-NFs.

immobilized particles. The shape of the curve suggests a Type IV isotherm, characteristic of mesoporous materials with average pore size of 5.1 Å in Mn and Mn-enzyme complex. The sharp uptake near $p/p_0 \approx 1.0$ is indicative of capillary condensation in mesopores, supported by mesoporosity. This indicates a pore shape *i.e.*, cylindrical or slit-like pores. The material exhibits mesoporosity with significant surface area and pore volume. On the other hand, the surface area of these self-assembled structures was found to be 58.89 m^2 g^{-1}. These findings confirm the formation of an assembly between the organic and inorganic components.[57]

The temperature and heat flow associated with the nanomaterial transitions as a function of time and temperature was done by differential scanning calorimetric (DSC) and thermal-gravimetric analysis (TGA). The weight loss in the case of MnPO$_4$ crystals was observed in two stages. The first weight loss was noted at around 80 °C that could be due to loss of water molecules. Up to 300 °C the weight loss could be due to the denaturation of the enzyme. The major weight loss (40%) was observed at around 300 °C and higher temperatures, which could be attributed to decomposition of metal phosphate crystals. In case of enzyme immobilized crystals, the proportion of weight loss was greater at 300 °C and higher temperatures, which could be due to decomposition of the organic component (*i.e.*, enzyme) of the nanoflower. The results validated the encapsulation of enzyme in manganese phosphate nano-crystals (Fig. 5C and D).[49,58]

The hydrodynamic size distribution of L-RI$_{Mn}$NFs suspended in buffer solution was determined by differential light scattering (DLS) (Fig. 6A). A uniform distribution of NFs was noted in the range of 700 to 900 nm. This size was close to the size determined by TEM analysis.[59] The stability of the suspended NFs was determined by measuring the surface charge distribution *i.e.*, zeta-potential of NFs. A shift in the zeta potential from −8.78 mV to +6.51 mV indicated loading of the enzyme onto the metal phosphate crystals forming aggregates in the form of NFs.[60]

The distribution of protein component in the L-RI$_{Mn}$NFs was analyzed by confocal laser scanning microscopy (CLSM). Fluorescently labelled protein emitted green spectra at around 525 nm. The NFs synthesized with labelled protein exhibited uniform distribution all over the nanoflower structure (Fig. 6C).[54,61] The spectrophotometric analysis showed the highest peaks at 230 and 280 nm, with estimated protein concentration of 0.156 mg ml^{-1} and a calculated enzyme load of 78% (Fig. 6B).

The activity assay was performed under the optimized reaction conditions for determining the conversion efficiency of L-RI$_{Mn}$NFs (Fig. S9A). The immobilized enzyme showed improved conversion over free enzyme, with almost 1.5 folds higher activity than the free counterpart. Since metal ions boost the activity of the enzymes, a system where framework is composed of favourable metal ions further improves the activity of the enzyme in the NFs. Such enhancement in the activity of the enzyme upon immobilization onto NFs has also been reported earlier.[50]

3.5. Effect of different reaction conditions

Determination of effect of temperature on activity and stability of an enzyme is a crucial factor for its long term and commercial application.[14] Immobilization of enzymes often improve the catalytic activity at higher temperatures.[62] Here, L-RI$_{Mn}$NFs exhibited activity in the temperature range of 50 °C to 95 °C with optima at 75 °C (Fig. 7A). Both free and immobilized enzyme showed an increment in the activity with increase in temperature, possibly due to rise in collisions of enzyme and substrate molecules favouring the mass transfer efficiency. But further increase in temperature led to drop in the activity for which disruption of protein conformation could be a major reason.[59] The immobilized enzyme clearly exhibited increased activity at elevated temperatures as compared to its free form. This behaviour of enzyme could be attributed to affirm incorporation of protein molecules into NFs, which perhaps protected the active site from harsh temperature conditions.[63]

Immobilized biocatalyst might face alteration in its pH activity profile.[64] However, in the present study, the immobilization of enzyme did not lead to any major change in the optimum pH. However, the pH stability of the enzyme was greatly improved as compared to its free counterpart, with highest stability at pH 6.0 and 7.0. The reason behind this could be a better shielding of the active site of the enzyme in acidic or alkaline environment. The

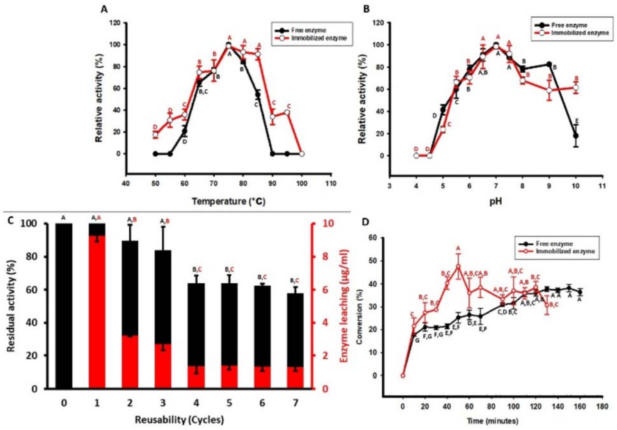

Fig. 7 Functional characterization of L-RI$_{\mathrm{Mn}}$NFs. (A) Comparative temperature profiles of free (LRI$_{\mathrm{M}}$) and immobilized (L-RI$_{\mathrm{Mn}}$NFs) enzyme, (B) comparative pH profiles of free (LRI$_{\mathrm{M}}$) and immobilized (L-RI$_{\mathrm{Mn}}$NFs) enzyme, (C) reusability of L-RI$_{\mathrm{Mn}}$NFs, and (D) time point conversion of D-allulose into D-allose by using free (LRI$_{\mathrm{M}}$) and immobilized (L-RI$_{\mathrm{Mn}}$NFs) enzyme. The mean values not sharing common letters are statistically different at P-value <0.05.

NFs exhibited substantial activity in the pH range of 5.0 to 10.0, achieving the maximum relative activity at neutral pH (Fig. 6B).[65]

3.6. Kinetic parameters of L-RI$_{\mathrm{Mn}}$NFs

The effect on the activity of enzyme immobilization onto hybrid nanoflowers was determined by applying the Michaelis–Menten kinetics and the Lineweaver–Burk equation. The $v_{\max}$ computed for the enzyme after NFs assembly was 2.14 µmole min^{-1}. The K_{m} value of the enzyme (64.44 mM) reduced to almost half after immobilization, indicating two-folds higher substrate affinity upon immobilization. This further led to improvement in other kinetic parameters. The turnover number (k_{cat}) and catalytic efficiency ($K_{\mathrm{m}}/k_{\mathrm{cat}}$) were also recorded to be increased by 2 and 3.5-folds, respectively, compared to its free counterpart. The calculated K_{m}, k_{cat} and $K_{\mathrm{m}}/k_{\mathrm{cat}}$ value were 64.44 mM, 679.9 s^{-1} and 10.55 M^{-1} s^{-1}, respectively, showing improvement in the kinetics of the immobilized enzyme (Table 1). This could be due various factors like affirm orientation of the enzyme, increased access to substrate molecules, reduced mass transfer resistance, *etc.* (Fig. S8).[66,67]

3.7. Reusability analysis

One of the major benefits of immobilization is in respect of industrial settings for its application to maximum advantage. The L-RI$_{\mathrm{M}}$ incorporated NFs retained their structure and were found to be functional up to 6 consecutive cycles, retaining more than 60% residual activity even after 6th reaction cycle (Fig. S9B). The later decrease in the activity (Fig. 7C) can be caused by either denaturation of the enzyme after consecutive uses or possible leaching of the enzyme after each cycle.[68]

Table 1 Kinetic parameters of free and nanoflower immobilized L-RIM

Kinetic parameter	Free enzyme	Immobilized enzyme
K_{m}	110 mM	64.44 mM
k_{cat}	328.8 s^{-1}	679.9 s^{-1}
$k_{\mathrm{cat}}/K_{\mathrm{m}}$	2.981 M^{-1} s^{-1}	10.55 M^{-1} s^{-1}

3.8. Bioconversion

The conversion of D-allulose into D-allose in the presence of NF incorporated enzyme showed increased yield as compared to the free counterpart. The maximum D-allulose to D-allose conversion of around 47% was recorded in nearly 50 min of catalytic reaction. Compared to free enzyme, about 10% additional conversion was recorded in less than half the time taken by the free enzyme (Fig. 7D). Moreover, the immobilization of L-rhamnose isomerase onto manganese-based nanoflowers presented here is the first report of this kind.[22,24,25] These observations clearly indicate the advancement and industrial feasibility of NFs for D-allose production.

4. Conclusions

In summary, L-rhamnose isomerase enzyme was successfully immobilized into a hybrid system of manganese and phosphate ions, to form flower-like nanostructures. The use of manganese ions as an inorganic component omitted the addition of Mn ions in the standard reaction. Incorporation of L-RI$_{\mathrm{M}}$ into nanoflowers bestowed better kinetic properties with 2 to 3.5-folds increase, as compared to its free counterpart. Further, D-allose biosynthesizing activity temperature was significantly improved from 55–90 °C to 50–95 °C, with 2 to 3-folds increase. On the other hand, activity in the alkaline pH range was improved by 3-folds. The benefit of easy preparation and separation of NFs by centrifugation helped in the reusability of NFs, retaining >60% activity after 6 consecutive reaction cycles. These results indicate that the nanoflowers are sustainable and green alternatives for the production of rare sugars such as D-allose.

Conflicts of interest

There are no conflicts to declare.

Data availability

The data supporting this article have been included as part of the supplementary information (SI). Supplementary information: synthesis of nanoflowers, molecular dynamic simulation, SEM and TEM micrographs of the nanoflowers, and comparative catalytic paremeters of immobilized L-rhamnose isomerases. See DOI: https://doi.org/10.1039/d5ra06127j.

Acknowledgements

Authors thank the Department of Biotechnology (DBT), Government of India, for financial support. SPS and SBS acknowledge the TATA Innovation Fellowship grant (HRD-16012/4/2024-HRD-DBT) and Gujarat Biotechnology University for all support. S. S. thanks University Grants Commission (UGC) for providing Senior Research Fellowship.

References

1 L. Sui, R. Nomura, Y. Dong, F. Yamaguchi, K. Izumori and M. Tokuda, *Cryobiology*, 2007, **55**, 87–92.

2 T. Nakamura, S. Tanaka, K. Hirooka, T. Toyoshima, N. Kawai, T. Tamiya, F. Shiraga, M. Tokuda, R. F. Keep, T. Itano and O. Miyamoto, *Neurosci. Lett.*, 2011, **487**, 103–106.

3 D. A. Bautista, R. B. Pegg and P. J. Shand, *J. Food Prot.*, 2000, **63**, 71–77.

4 D. Gao, N. Kawai, T. Nakamura, F. Lu, Z. Fei and T. Tamiya, *Neurol. Med.-Chir.*, 2013, **53**, 365–374.

5 S. Khajeh, M. Ganjavi, G. Panahi, M. Zare, M. Zare, S. M. Tahami and V. Razban, *Curr. Mol. Pharmacol.*, 2022, **16**, 801–810.

6 K. Takao, M. Suzuki, R. Miyazaki, M. Miyake, K. Akimitsu and K. Hoshino, *Biochem. Biophys. Res. Commun.*, 2022, **627**, 130–136.

7 M. A. Hossain, H. Wakabayashi, F. Goda, S. Kobayashi, T. Maeba and H. Maeta, *Transplant. Proc.*, 2000, **32**, 2021–2023.

8 A. Taborda, M. Renio, M. R. Ventura and L. O. Martins, *Green Chem.*, 2025, **27**, 1044–1053.

9 M. N. Choi, K. C. Shin, D. W. Kim, B. J. Kim, C. S. Park, S. J. Yeom and Y. S. Kim, *Front. Bioeng. Biotechnol.*, 2021, **9**, 681253.

10 W. Mu, W. Zhang and Q. Chen, *Novel Enzymes for Functional Carbohydrates Production: from Scientific Research to Application in Health Food Industry*, 2021, pp. 1–289.

11 W. Bai, J. Shen, Y. Zhu, Y. Men, Y. Sun and Y. Ma, *Food Sci. Technol. Res.*, 2015, **21**, 13–22.

12 K. Xu, B. Appiah, B. W. Zhang, Z. H. Yang and C. Quan, *J. Catal.*, 2023, **418**, 31–39.

13 Z. Wang, R. Wang, Z. Geng, X. Luo, J. Jia, S. Pang, X. Fan, M. Bilal and J. Cui, *Crit. Rev. Biotechnol.*, 2024, **44**, 674–697.

14 M. Mohammadi, S. Gandomkar, Z. Habibi and M. Yousefi, *RSC Adv.*, 2016, **6**, 52838–52849.

15 G. Dik, B. Bakar, A. Ulu and B. Ateş, *Ind. Eng. Chem. Res.*, 2023, **62**, 14111–14129.

16 S. Shompoosang, A. Yoshihara, K. Uechi, Y. Asada and K. Morimoto, *Biosci. Biotechnol. Biochem.*, 2014, **78**, 317–325.

17 C. Li, L. Gao, K. Du, H. Lin, Y. Ren, J. Lin and J. Lin, *Bioprocess Biosyst. Eng.*, 2020, **43**, 645–653.

18 Y. S. Kim, K. C. Shin, Y. R. Lim and D. K. Oh, *Biotechnol. Lett.*, 2013, **35**, 259–264.

19 B. T. Menavuvu, W. Poonperm, K. Leang, N. Noguchi, H. Okada, K. Morimoto, T. B. Granström, G. Takada and K. Izumori, *J. Biosci. Bioeng.*, 2006, **101**, 340–345.

20 N. R. Mohamad, N. H. C. Marzuki, N. A. Buang, F. Huyop and R. A. Wahab, *Biotechnol. Biotechnol. Equip.*, 2015, **29**, 205–220.

21 H. T. Imam, P. C. Marr and A. C. Marr, *Green Chem.*, 2021, **23**, 4980–5005.

22 Y. Hu, G. Xu, M. S. Robescu and T. Bavaro, *Molecules*, 2025, **30**, 939.

23 Z. Lei, C. Gao, L. Chen, Y. He, W. Ma and Z. Lin, *J. Mater. Chem. B*, 2018, **6**, 1581–1594.

24 K. A. Al-maqdi, M. Bilal, A. Alzamly, H. M. N. Iqbal, I. Shah and S. S. Ashraf, *Nanomaterials*, 2021, **11**, 1460.

25 S. W. Lee, S. A. Cheon, M. Il Kim and T. J. Park, *J. Nanobiotechnol.*, 2015, **13**(1), 1–10.

26 X. Liang, Y. Liu, K. Wen, W. Jiang and Q. Li, *J. Mater. Chem. B*, 2021, **9**, 7597–7607.

27 Y. N. Reddy, A. De, S. Paul, A. K. Pujari and J. Bhaumik, *Biomacromolecules*, 2023, **24**, 1717–1730.

28 J. C. S. Terra, A. R. Martins, F. C. C. Moura, C. C. Weber and A. Moores, *Green Chem.*, 2022, **24**, 1404–1438.

29 E. R. Engel, E. R. Engel and J. L. Scott, *Green Chem.*, 2020, **22**, 3693–3715.

30 Z. F. Wu, Z. Wang, Y. Zhang, Y. L. Ma, C. Y. He, H. Li, L. Chen, Q. S. Huo, L. Wang and Z. Q. Li, *Sci. Rep.*, 2016, **6**(1), 1–7.

31 J. Ge, J. Lei and R. N. Zare, *Nat. Nanotechnol.*, 2012, **7**, 428–432.

32 H. S. Jamal, R. Raja, S. Ahmed, G. Yesiloz and S. A. Ali, *Int. J. Biol. Macromol.*, 2024, **274**, 133114.

33 S. Sharma, S. N. Patel and S. P. Singh, *Appl. Microbiol. Biotechnol.*, 2024, **108**, 1–13.

34 M. J. Abraham, T. Murtola, R. Schulz, S. Páll, J. C. Smith, B. Hess and E. Lindah, *SoftwareX*, 2015, **1–2**, 19–25.

35 R. B. Best, X. Zhu, J. Shim, P. E. M. Lopes, J. Mittal, M. Feig and A. D. MacKerell, *J. Chem. Theory Comput.*, 2012, **8**, 3257–3273.

36 R. Manjunatha Kini and H. J. Evans, *J. Biomol. Struct. Dyn.*, 1991, **9**, 475–487.

37 T. Darden, D. York and L. Pedersen, *J. Chem. Phys.*, 1993, **98**, 10089–10092.

38 B. Hess, H. Bekker, H. J. C. Berendsen and J. G. E. M. Fraaije, *J. Comput. Chem.*, 1997, **18**, 1463–1472.

39 N. Rana, D. Patel, M. Parmar, N. Mukherjee, P. C. Jha and A. Manhas, *Sci. Rep.*, 2023, **13**, 1–22.

40 F. R. Salsbury, *Curr. Opin. Pharmacol.*, 2010, **10**, 738–744.

41 X. N. Peng, J. Wang and W. Zhang, *Oncol. Lett.*, 2017, **14**, 2244–2248.

42 E. Durham, B. Dorr, N. Woetzel, R. Staritzbichler and J. Meiler, *J. Mol. Model.*, 2009, **15**, 1093–1108.

43 S. Rampogu, G. Lee, J. S. Park, K. W. Lee and M. O. Kim, *Int. J. Mol. Sci.*, 2022, **23**, 1771.

44 Z. Ashkan, R. Hemmati, A. Homaei, A. Dinari, M. Jamlidoost and A. Tashakor, *Int. J. Biol. Macromol.*, 2021, **168**, 708–721.

45 H. Yoshida, M. Yamada, Y. Ohyama, G. Takada, K. Izumori and S. Kamitori, *J. Mol. Biol.*, 2007, **365**, 1505–1516.

46 Z. Wang, P. Liu, Z. Fang and H. Jiang, *Int. J. Mol. Sci.*, 2022, **23**, 11853.

47 S. Lambhiya, G. Patel and U. C. Banerjee, *Bioresour. Bioprocess.*, 2021, **8**, 1–14.

48 L. Duan, H. Li and Y. Zhang, *ACS Omega*, 2018, **3**, 18234–18241.

49 J. C. Munyemana, H. He, S. Ding, J. Yin, P. Xi and J. Xiao, *RSC Adv.*, 2018, **8**, 2708–2713.

50 S. K. Rai, L. K. Narnoliya, R. S. Sangwan and S. K. Yadav, *ACS Sustain. Chem. Eng.*, 2018, **6**, 6296–6304.

51 Y. Huang, X. Ran, Y. Lin, J. Ren and X. Qu, *Chem. Commun.*, 2015, **51**, 4386–4389.

52 S. Soni, B. P. Dwivedee and U. C. Banerjee, *ChemNanoMat*, 2018, **4**, 1007–1020.

53 Z. Zhang, Y. Zhang, R. Song, M. Wang, F. Yan, L. He, X. Feng, S. Fang, J. Zhao and H. Zhang, *Sens. Actuators, B*, 2015, **211**, 310–317.

54 H. Zhu, J. Chen, Y. Zhang, K. L. Goh, C. Wan, D. Zheng and M. Zheng, *Int. J. Biol. Macromol.*, 2023, **246**, 125622.

55 V. Sharmila and M. Parthibavarman, *J. Mater. Sci.: Mater. Electron.*, 2019, **30**, 19813–19825.

56 Z. Y. Liu, G. T. Fu, L. Zhang, X. Y. Yang, Z. Q. Liu, D. M. Sun, L. Xu and Y. W. Tang, *Sci. Rep.*, 2016, **6**(1), 1–10.

57 S. J. Lee, H. Jang and D. N. Lee, *Nanoscale Adv.*, 2023, **5**, 5165–5213.

58 J. Gao, H. Liu and C. Tong, *Inorg. Chem.*, 2023, **62**, 13812–13823.

59 S. Anboo, S. Y. Lau, J. Kansedo, P. S. Yap, T. Hadibarata and A. H. Kamaruddin, *Heliyon*, 2024, **10**, e27348.

60 X. Shen, Q. Wang, Y. Liu, W. Xue, L. Ma, S. Feng, M. Wan, F. Wang and C. Mao, *Sci. Rep.*, 2016, **6**, 1–9.

61 S. Zhang, H. Sun, Z. Huang, Z. Han, J. Hou, F. Lu and Y. Liu, *Fermentation*, 2023, **9**, 1016.

62 Y. R. Maghraby, R. M. El-Shabasy, A. H. Ibrahim and H. M. E. S. Azzazy, *ACS Omega*, 2023, **8**, 5184–5196.

63 M. Mostafavi, M. B. Poor, Z. Habibi, M. Mohammadi and M. Yousefi, *Int. J. Biol. Macromol.*, 2024, **254**, 127817.

64 G. Rilievo, A. Cecconello, S. Molinari, A. Venerando, L. Rutigliano, G. T. Govardhan, D. H. Kariyawasam, R. J. Arusei, L. Zennaro, M. L. Di Paolo, E. Agostinelli, F. Vianello and M. Magro, *Int. J. Mol. Sci.*, 2022, **23**, 12172.

65 C. Gulmez, C. Altinkaynak, M. Ozturkler, N. Ozdemir and O. Atakisi, *J. Biosci. Bioeng.*, 2021, **132**, 327–336.

66 S. A. Ahmed, F. A. Mostafa and M. A. Ouis, *Int. J. Biol. Macromol.*, 2018, **112**, 371–382.

67 S. A. Ahmed, S. A. A. Saleh, S. A. M. Abdel-Hameed and A. M. Fayad, *Heliyon*, 2019, **5**, e01674.

68 M. Mostafavi, K. Mahmoodzadeh, Z. Habibi, M. Yousefi, J. Brask and M. Mohammadi, *Int. J. Biol. Macromol.*, 2023, **230**, 123140.